



Full length article

Indocyanine green modified silica shells for colon tumor marking

Adrian Garcia Badaracco^a, Erin Ward^b, Christopher Barback^c, Jian Yang^d, James Wang^a, Ching-Hsin Huang^a, Moon Kim^e, Qingxiao Wang^e, Seungjin Nam^e, Jonathan Delong^b, Sarah Blair^b, William C. Trogler^d, Andrew Kummel^{d,*}

^a Department of Nanoengineering, University of California, San Diego, 9500 Gilman Drive, La Jolla, CA 92093, United States

^b Department of Surgery, University of California, San Diego, 9500 Gilman Drive, La Jolla, CA 92093, United States

^c Department of Radiology, University of California, San Diego, 9500 Gilman Drive, La Jolla, CA 92093, United States

^d Department of Chemistry and Biochemistry, University of California, San Diego, 9500 Gilman Drive, La Jolla, CA 92093, United States

^e Department of Materials Science and Engineering, The University of Texas at Dallas, 800 West Campbell Road, Richardson, TX 75080, USA



ARTICLE INFO

Keywords:

Indocyanine green
India ink
Tumor marking
Silica shell
Heterogeneous dye
Self-quenching

ABSTRACT

Marking colon tumors for surgery is normally done with the use of India ink. However, non-fluorescent dyes such as India ink cannot be imaged below the tissue surface and there is evidence for physiological complications such as abscess, intestinal perforation and inconsistency of dye injection. A novel infrared marker was developed using FDA approved indocyanine green (ICG) dye and ultrathin hollow silica nanoshells (ICG/HSS). Using a positively charged amine linker, ICG was non-covalently adsorbed onto the nanoparticle surface. For ultra-thin wall 100 nm diameter silica shells, a bimodal ICG layer of < 3 nm is formed. Conversely, for thicker walls on 2 μm diameter silica shells, the ICG layer was only bound to the outer surface and was 6 nm thick. In vitro testing of fluorescent emission showed the particles with the thinner coating were considerably more efficient, which is consistent with self-quenching reducing emission shown in the thicker ICG coatings. Ex-vivo testing showed that ICG bound to the 100 nm hollow silica shells was visible even under 1.5 cm of tissue. In vivo experiments showed that there was no diffusion of the ICG/nanoparticle marker in tissue and it remained imageable for as long as 12 days.

1. Introduction

Locating small colon cancers intraoperatively can be both challenging and technically difficult. Colonoscopy based tumor tattooing allows for most colon tumors to be identified and marked pre-operatively to facilitate accurate surgical excisions. With current technology, at the time of colonoscopy, either a biopsied polyp or mass can be marked inside the colon to allow the surgeon to locate the tumor. This technique is particularly helpful for small lesions that are not palpable or visible from the outside of the colon. The use of preoperative tattooing is particularly critical during laparoscopic or robotic cases when the tactile sense of the surgeon is limited secondary to the instrumentation [1,2].

Currently the mainstay of endoscopy based preoperative tattooing is done with India ink. While India ink is well established as a reliable way to mark lesions in the colon, there are reports of instances when India ink is associated with side effects including colonic abscess, intestinal infarction and intestinal perforation, with incidences of some reported to be as high as 14.3% [3–7]. Furthermore, imaging is restricted to the

tissue surface since India ink is imaged by visible light adsorption. In addition to the possible side effects related to the use of India ink, there have been reports of tattoo failure in 15% to 31.5% of cases [8]. When these issues arise, they may lead to additional colonoscopies or even resection of the unnecessary section of the colon [9]. At present, minimal effective alternatives to India ink exist.

Recently, Indocyanine green (ICG) has been proposed as an alternative bioimaging agent due to its biocompatibility and high tissue optical penetration depth at near IR wavelengths. ICG is a tricarbo-cyanine dye that has strong absorption and emission maxima at ≈ 780 and ≈ 820 nm, respectively [10]. ICG has low toxicity [11], is approved by FDA, and is widely used for optical imaging applications in the clinic [12–14]. The use of intraoperative ICG continues to grow as an increasing number of commercially available laparoscopic and robotic systems have cameras capable of imaging ICG fluorescence [15]. By minimizing incision sizes, laparoscopic surgery leads to superior surgical outcomes and shorter recovery periods, but due to the loss of tactile feedback it requires precise pre-operative marking [1,2,8]. ICG is also reported to be used for other medical applications, such as

* Corresponding author.

<https://doi.org/10.1016/j.apsusc.2019.143885>

Received 11 March 2019; Received in revised form 15 August 2019; Accepted 4 September 2019

Available online 05 September 2019

0169-4332/ © 2019 Elsevier B.V. All rights reserved.

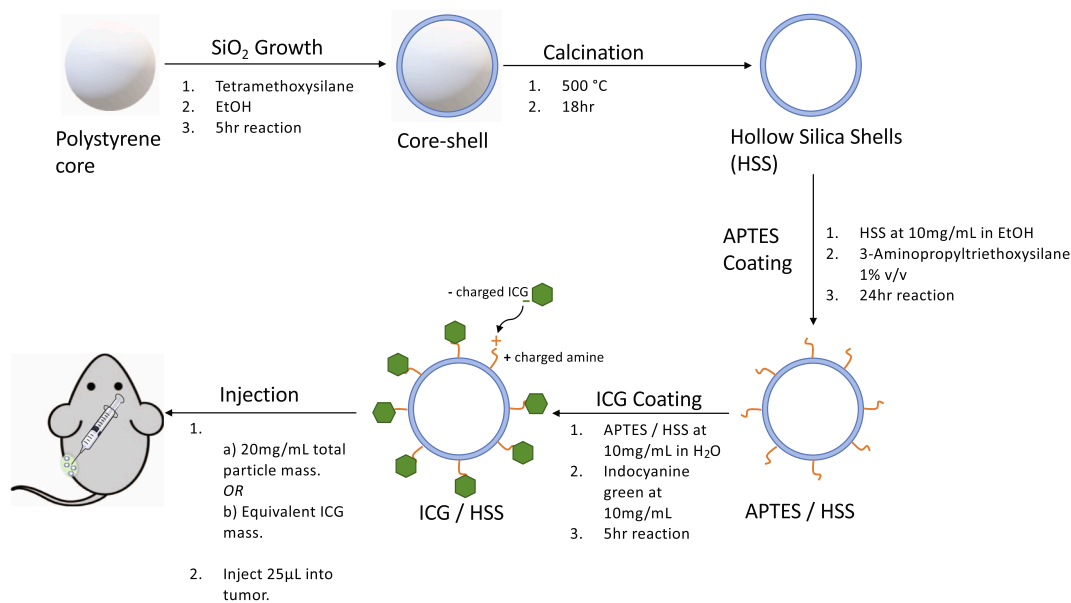


Fig. 1. Preparation of ICG@HSS: First, a polystyrene core was covered with a thin layer of silica to yield a core-shell structure as described in Ref. 34. Second, calcination was used to remove the sacrificial polystyrene core to produce a plain ultrathin hollow silica shell (UHSS). Third, to coat with ICG, UHSS were suspended at 10 mg/mL in pure ethanol and 10 μ L of APTES was added (1% v/v). This solution was shaken vigorously for 24 h, followed by 2 washes with ethanol and 2 washes with water to remove any unreacted APTES. Fourth, 10 mg of ICG dye were added to this solution and shaken for 5 h to yield ICG-loaded UHSS (ICG/HSS). The resultant ICG/UHSS were purified by washing with water until the supernatant was colorless. Fifth, tumor injections were performed with either 25 μ L of a 20 mg/mL suspension of ICG/HSS in water or 25 μ L of the ICG control in water with the same total ICG concentration.

photoacoustic imaging, [16–18] photothermal [19–22] and photodynamic therapies [23]. Because of its existing widespread use in surgery and well-established safety profile, ICG dye could be a viable alternative to India ink for tattooing of tumors.

Although ICG is cleared from circulation in < 5 min when injected intravenously due to protein and phospholipid binding, [24,25] it has been reported to persist for several days when injected intratumorally (IT) and previous studies have shown that ICG can serve as a safe colonic tumor marker [3,7,26–28]. Despite this promise, other studies have shown that ICG alone may be inferior to India ink because > 40% of ICG markings were not visible after 2 weeks [3,26–28]. Since ICG is a small molecule, it may diffuse through tissues or be reabsorbed and lose visibility, especially under visible wavelengths. ICG also suffers from low water solubility and self-quenching by aggregation [29,30].

To overcome these limitations, ICG has been incorporated into polymeric or metal nanoparticles, thus shielding the ICG from proteins and degradation in water [18,20,21,30,31]. Lee et al. reported binding of ICG on the surface of mesoporous silica nanoparticles (MSN) to study the biodistribution of MSN. The surface of silica particles was pre-treated with 3-aminopropyltrimethoxysilane and ICG molecules were electrostatically adsorbed to the positive amine functional groups. The adsorbed ICG dye was stable in water over a pH range from 3.0 to 10.0. Lee et al. also reported on the biodistribution of ICG coated silica shells. Six hours after IV injection, most of the particles accumulate in the liver (35.3%) with < 10% in other major organs [25]. A summary of existing literature regarding the use of nanoparticles and ICG as a tumor marker is tabulated in Fig. S1.

Previously, hollow silica shells with a diameter ranging from 100 nm to 2 μ m and their application as ultrasound contrast agent has been reported [32–40]. Because of the synthesis of the shell is performed on the surface of well characterized templates, the shells have a narrow size distribution and, are better suited for medical applications [39,40]. These ultrathin silica shells have also been shown to be biocompatible with a good safety profile [41]. In the present study, the synthesis and testing of ICG coated silica shells that overcome some of the limitations of free ICG dye is presented. By adsorbing thin ICG

layers to amine surface functionalized hollow silica nanoshells, high fluorescent brightness and low tissue mobility are achieved for the marker. These show promise as an adjunct or replacement for the standard India ink marker due to the proven safety profile of ICG dye, the ease of visualization even when injected under 1 cm of tissue, and immobilization at the site of injection for longer duration marking.

2. Methods

2.1. Preparation of ICG loaded shells

3-Aminopropyltriethoxy silane (APTES) and indocyanine green (ICG) were purchased from Sigma-Aldrich (St. Louis, MO). The 100 nm and 2 μ m polystyrene beads were purchased from Polysciences (Warrington, PA). 100 nm silica nanoshells and 2 μ m boron-doped silica microshells were synthesized as described previously [36,37,41].

First, APTES was attached to the silica shell. To achieve this, 1 mL of 10 mg/mL of 100 nm or 2 μ m silica shells suspended in 100% ethanol were mixed with 10 μ L of APTES to form a 1% v/v APTES/ethanol solution with suspended UHSS. This suspension was shaken vigorously for 24 h and washed twice with ethanol and twice with water to remove unbound APTES, yielding APTES/HSS. Centrifugation for 5 min at 5000 rpm was used for all purification washes.

Second, to coat the UHSS with ICG, the APTES/HSS were centrifuged for 5 min at 5000 rpm and resuspended at 10 mg/mL in 1 mL of a 10 mg/mL ICG water solution (ICG to silica shell ratio of 1:1 by mass). Afterwards, the APTES/HSS/ICG were vortex mixed for 5 h at room temperature in a dark environment. ICG/HSS were collected by centrifugation for 5 min at 5000 rpm. The pellet was washed at least three times with water or until the supernatant was colorless. The washed ICG/HSS were re-suspended in water at 20 mg/mL. These samples were kept frozen and shielded from light during storage. (See Fig. 1)

2.2. Quantification of ICG and imaging of the shells

Quantification of ICG loading on the UHSS was performed by

measuring the absorption of ICG/HSS in water at 780 nm on a Perkin Elmer Lambda 35 UV-Vis Spectrophotometer. In order to release the dye from the shells, the ICG/HSS were suspended in a 1% Tween20 solution as previously described by Hong et al. [40]. The standard curve was made with the absorption of ICG water solution as a function of ICG concentration. When the absorption of ICG coated silica shells in water was measured, non-modified silica shells in water suspension at the same concentration were used as a blank to correct for the scattering absorption. Measurement of fluorescence intensity was performed using an IR camera (Fluobeam-800, Fluoptics, Grenoble, France) at a distance of 15 cm.

Combined field emission SEM (FESEM) images were obtained using a Sigma 500 FE-SEM (Zeiss, Germany) with an accelerating voltage ranging from 0.8 to 20 kV. SEM samples were prepared by depositing silica shells on a carbon tape substrate.

Transmission electron microscopy (TEM) and scanning transmission electron microscopy (STEM) characterization was performed using a spherical aberration (Cs) corrected JEM-ARM200F electron microscope (JEOL USA INC) operated at 200 kV. The convergence semiangle of the electron probe was set to 25 mrad with an electron probe current of 23 pA. High angle annular dark field (HAADF) and annular bright field (ABF) imaging was carried out with the collection semiangle from 70 to 250 mrad and 12–24 mrad, respectively. Electron energy loss spectroscopy (EELS) was performed using an Enfina spectrometer (Gatan Inc.) with a collection semiangle of 30 mrad. 0.2 s/pixel was used for the elemental mapping of C and O using EELS. Quantification of layer thickness in Fig. 5 and Fig. 6 was performed using MATLAB. Upscaling and a gaussian blur were applied before final quantification in order to remove the high noise visible in Fig. S2.

2.3. Chemical stability

To explore the chemical stability of ICG adsorbed to silica, ICG/HSS were centrifuged, the supernatant was removed, and the ICG/HSS were resuspended in either pH 4.0 buffer (potassium acid phthalate) (Fischer Scientific, New Jersey, USA) or pH 10.0 buffer (potassium carbonate-potassium borate-potassium hydroxide) (Fischer Scientific, New Jersey, USA). After storing overnight at room temperature, the shells were spun down and the supernatant's UV-Vis spectrum was measured to quantify the remaining ICG dye in solution. Blanks of the corresponding buffers were used for the UV-Vis spectra.

Degradation of ICG dye adsorbed onto amine functionalized silica shells was measured in-vitro by suspending ICG loaded shells in water at 0.05 mg/mL and storing in a dark environment. Free ICG dye in water at a concentration of 2 µg/mL was used as a control. Emission at 800 nm was monitored for several days by placing the samples under an IR camera (Fluobeam-800, Fluoptics, Grenoble, France) at a standard distance of approximately 15 cm.

2.4. Ex vivo phantom testing

100 nm ICG/HSS were diluted to 0.25 mg/mL in DI water and 2 mL of this sample was placed under the IR camera at a 15 cm distance. Afterwards, several layers of chicken or beef tissue were layered on top of the samples, mimicking tissue injections at varying depths. After all the tissue layers were stacked, the sample was removed, and background images were taken. All images were taken using a fixed exposure time of 200 ms.

After background subtraction was performed, mean intensity of the sample area was measured. All statistical analysis and plotting were performed with Microsoft Excel and MATLAB while intensity measurements were performed using ImageJ.

2.5. In vivo toxicology

All animal studies were approved by UC San Diego Institutional

Animal Care and Use Committee (UCSD IACUC). Healthy 6–8-week-old female BALB/c mice ($n = 3$) were intravenously injected with 150 mg/kg plain 100 nm SiO₂ nanoshells to measure systematic toxicity. 24 h after injection, 400 µL of blood was collected and put into tubes pre-coated with ethylenediaminetetraacetic acid (EDTA) as an anticoagulant. The tubes were immediately flicked and inverted several times to distribute the EDTA/blood and then analyzed using a Hemavet 950FS cell counter (Drew Scientific Inc., Miami Lakes, USA). All samples were measured twice in duplicate.

2.6. In vivo testing

All animal studies were approved by UCSD IACUC. Single flank tumors were established in five C57 wildtype mice with GL261 cell line. Cells were grown from frozen for 2 passes over the course of 2–3 weeks in a completed Dulbecco's Modified Eagle Medium (DMEM)/F12 culture medium. Complete medium was prepared as follows: 5 mL of Penstrip (Gibco, Cat#15140–122), 5 mL of Glutamax (Gibco), 1 mL of 10 µg/mL Fibroblast Growth Factor (FGF, STEMCELL Technologies), 1 mL of 10 µg/mL Epidermal Growth Factor (EGF, STEMCELL Technologies) were added into one bottle of DMEM/F12 media (Gibco). To establish these tumors, 1×10^6 cells were subcutaneously injected into the flanks of anesthetized mice and allowed to grow for about two weeks to achieve an average of 217 mm³ tumor volume. Four of the mice were injected with 25 µL of 20 mg/mL 100 nm ICG particles at about 0.25–0.5 cm depth. An additional four mice had 25 µL of a 1 mg/mL solution of pure ICG in water injected into the tumor at the same depth. Serial images of the tumor were taken on post-injection days 3, 5, 7, 10, 13, 15, 18 and 21. Mice injected with ICG/HSS and free ICG dye were imaged on the same schedule and with a single-blind protocol.

3. Results and discussion

3.1. Characterization of ICG coated silica shells

3.1.1. Chemical stability

ICG coated silica shells were prepared by adsorbing anionic ICG dye to an ultrathin hollow silica shell. Silica shells were prepared using protocols previously described [36,37,41]. ICG coating was achieved by first attaching 3-aminopropyltriethoxy silane (APTES) to the silica to impart a cationic surface charge to the shell. Then, negatively charged ICG dye molecules are adsorbed onto the shell by electrostatic attraction. In order to test the stability of the electrostatic bond, incubation of ICG loaded shells in pH 4 and pH 10 buffer overnight revealed no free ICG dye in solution, indicating that the electrostatic adsorption of the dye is stable under physiological conditions. This agrees with previous results from Lee et al. with similarly functionalized mesoporous silica particles [25].

ICG is well known to degrade in solution, with the rate of degradation depending on factors such as solvent, concentration and temperature [24]. Saxena et al. reported that in water at room temperature, ICG degrades with pseudo first-order kinetics and a $t_{1/2}$ of 16.8 h⁻¹ at 1 µg/mL [42]. Using the model provided by Saxena et al., the decay in emission intensity over time can be represented by an eq. (1), where I is the emission intensity at time t , I_0 is the emission intensity at $t = 0$ and k is the observed decay constant:

$$I = I_0 \exp(-kt) \quad (1)$$

The half-life ($t_{1/2}$) can then be calculated from the observed decay constant according to Eq. (2), where k is the observed decay constant from Eq. (1):

$$t_{1/2} = \frac{0.693}{k} \quad (2)$$

From the plots in Fig. S3, the $t_{1/2}$ for free ICG dye in room temperature water at a concentration of 2 µg/mL was found to be

approximately 16.6 h^{-1} . This result agrees with the lifetime reported by Saxena et al. ICG coated nanoshells also exhibited an exponential degradation pattern but the lifetime was extended to 56.4 h^{-1} . This indicates that adsorption of ICG dye to shells offers some protection against chemical degradation but does not completely shield the dye from the environment.

3.1.2. Imaging of coated and uncoated shells

The geometrical nature of bare hollow silica shells is shown in Fig. 2. Both 100 nm nanoshells and $2 \mu\text{m}$ microspheres have thin walls and a hollow central cavity. For the 100 nm shells, the SEM image (Fig. 2a) shows the shell diameters are uniform and consistent across a large population of nanoshells. Fig. 2b shows TEM images of the 100 nm nanoshells. For the 100 nm nanoshells, the wall thickness appears to be non-uniform relative to the diameter of the particle, which is consistent with a porous self-assembled nanoparticle [43]. The shell walls appear dark due to high density SiO_2 in the wall while the interior of the shells appears translucent because of the hollow nature of the core. Fig. 2c shows SEM images for the $2 \mu\text{m}$ hollow SiO_2 shells. The $2 \mu\text{m}$ microspheres appear to have thicker walls than the 100 nm nanoshells, but they also appear uniform in diameter. Fig. 2d shows TEM images for the $2 \mu\text{m}$ microspheres and highlights the very thin walls relative to the diameter of the particles. Although the $2 \mu\text{m}$ hollow SiO_2 shells have thin and smooth walls, a small amount of colloidal silica is observed on the shell surface, appearing as small white particulates in the SEM image (Fig. 2c) and darker spheres or aggregates in the TEM image (Fig. 2d) adhered to the outside of the shell. These observations indicate that both 100 nm nanoshells and $2 \mu\text{m}$ microspheres are of uniform diameter and consist of a thin silica wall with a hollow interior space formed by templated self-assembly of sol particulates.

Fig. 3 shows TEM images of the silica shells with and without ICG. The panels on the left show TEM images of bare or ICG coated silica shells, while the panels on the right give schematic diagrams of the

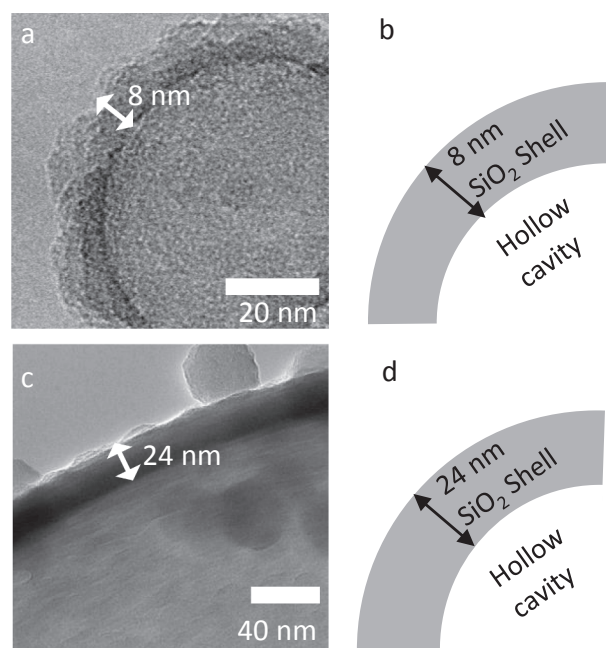


Fig. 3. TEM images of SiO_2 Nanoshell Walls: (a) TEM image of uncoated 100 nm nanoshells showing an SiO_2 thickness of approximately 8 nm and (b) schematic representation of the TEM image to aid understanding of the layers and relation to the hollow space. (c) TEM image of an uncoated shell for a $2 \mu\text{m}$ shell with an SiO_2 layer that is about 24 nm thick, (d) schematic of the TEM image showing the relative position of the hollow cavity inside the shell.

layers observed on TEM to assist interpretation. Fig. 3a shows a single uncoated 100 nm nanoshell with a wall thickness of about 8 nm. As seen in the schematic of Fig. 3b, this is a single SiO_2 layer encapsulating the hollow core of the particle. This comparison process is repeated for the $2 \mu\text{m}$ microspheres. In Fig. 3c, the uncoated $2 \mu\text{m}$ microspheres exhibit an approximate 24 nm wall thickness. Per the schematic in Fig. 3d, the wall is composed of a solid 24 nm SiO_2 layer encapsulating the hollow interior space; although in the TEM image the SiO_2 layer has regions of higher and lower density (based on the darkness of the shell) as well as large colloidal particles, like the ones seen in the top right of Fig. 3c [39]. The thickness of these layers as well as the thickness after coating with ICG was confirmed by elemental mapping by TEM-EELS, as described in Figs. 5 and 6 for 100 nm nanoshells and $2 \mu\text{m}$ microspheres, respectively.

Evaluation of in vitro brightness is shown in Fig. 4. Fig. 4a compares dye loading for $2 \mu\text{m}$ microspheres and 100 nm nanoshells. The loading of ICG on silica shells was calculated to be at minimum $54 \mu\text{g}/\text{mg}$ for $2 \mu\text{m}$ microspheres and $43 \mu\text{g}/\text{mg}$ for the 100 nm nanoshells. This method has previously been shown to allow order of magnitude measurement of heterogeneous ICG dye concentrations, but underestimates loading due to absorption quenching [40]. Because the measured dye loadings are within 20% of each other, comparison between the two sizes of particles is reasonable. Consequently, all further experiments were performed controlling for total mass instead of ICG dye mass.

To compare the emission intensity of the shells, they were suspended at $0.25 \text{ mg}/\text{mL}$ and $0.025 \text{ mg}/\text{mL}$ (mass of SiO_2 /volume of DI water) and imaged using the use of an infrared CCD camera. Two comparisons were measured: differences in brightness between particle sizes are shown in panels 3b and 3c and changes in brightness due to concentration are shown in panels 3d and 3e. Raw images used in the calculations are shown in Fig. S4. The intensity values are the mean intensity within a region of interest (ROI) while error bars represent standard deviations of intensity within ROI. Fig. 4b shows that at $0.25 \text{ mg}/\text{mL}$, 100 nm nanoshells are $10\times$ brighter than $2 \mu\text{m}$ microspheres, while Fig. 4c shows that at a lower concentration of $0.025 \text{ mg}/$

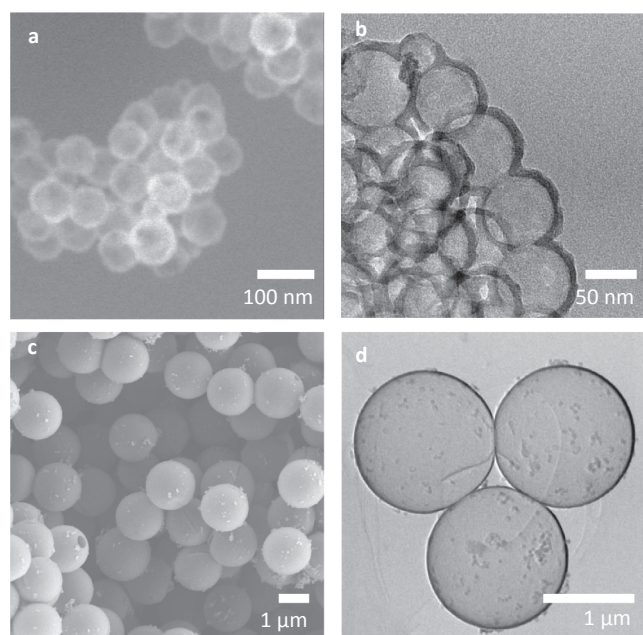


Fig. 2. Representative EM images of uncoated SiO_2 Nanoshells: (a) SEM images of 100 nm of hollow SiO_2 nanoshells showing uniform diameter shells and (b) TEM images of the 100 nm SiO_2 nanoshells. 100 nm nanoshells have thin walls (dark, dense region) along with hollow interior space (light region). The walls on the 100 nm nanoshells exhibit some non-uniformity relative to the diameter of the particles. (c) SEM images of $2 \mu\text{m}$ hollow SiO_2 microspheres. $2 \mu\text{m}$ microspheres have uniform diameters and, unlike 100 nm nanoshells, have some colloidal silica on the surface. (d) TEM images of the $2 \mu\text{m}$ microspheres showing very uniform thin shell walls relative to the particle diameter.

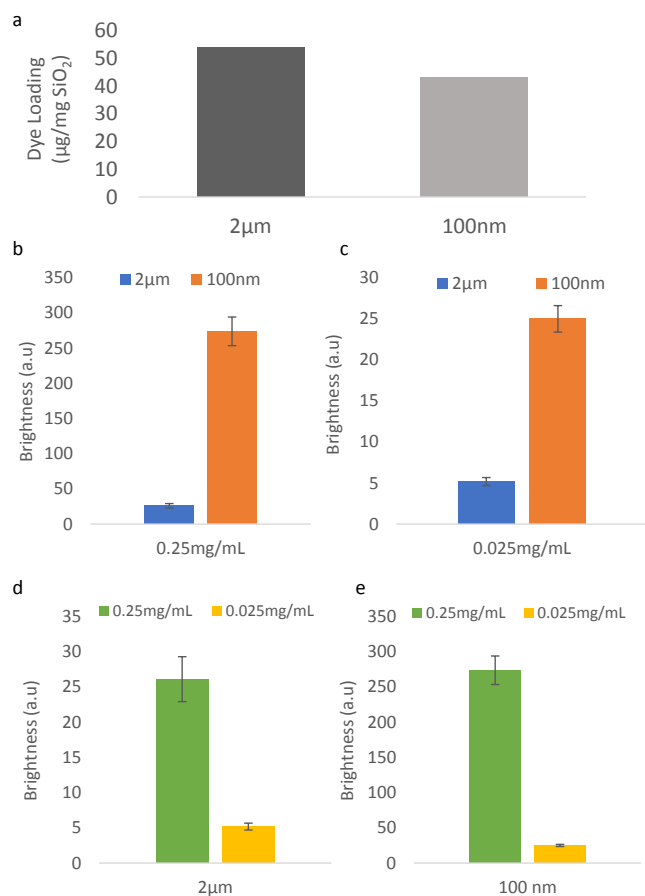


Fig. 4. Brightness of 100 nm ICG coated shells compared to 2µm ICG coated shells. (a) Comparison of dye loading between 100 nm nanoshells and 2µm microshells. Dye loading was measured by suspending the ICG coated shells in a water solution at 0.1 mg/mL and measuring absorption against a free ICG dye calibration curve. Loading was found to be 54 µg/mg for 2µm shells and 43 µg/mg for 100 nm shells. (b) Comparison of fluorescent emission intensity at 0.25 mg/mL SiO₂ mass concentration. 100 nm nanoshells are 10× brighter than the larger 2µm shells, despite similar bulk ICG concentration (c) Comparison of fluorescent emission intensity at 0.25 mg/mL SiO₂ mass concentration. 100 nm shells are 5× brighter than the 2µm shells. (d) Comparison between 0.25 mg/mL and 0.025 mg/mL for 2µm shells. 2µm shells show a 5× increase in signal strength with a 10× increase in in microshell concentration, suggesting possible self-quenching. (e) Comparison between 0.25 mg/mL and 0.025 mg/mL for 100 nm shells. 100 nm nanoshells exhibit 10× brightness with 10× concentration increase, a linear increase. Raw images for this data are shown in Fig. S4.

mL, 100 nm nanoshells are only 5× brighter than 2µm microshells. In order to explore the concentration dependence of brightness in the range examined, samples of the same size silica shell are compared. Fig. 4d shows that 2µm microshells increase in brightness 5× with a 10× increase in concentration, which suggests inter-particle self-quenching at particle mass loadings of 0.25 mg/mL. For the 100 nm nanoshells, Fig. 4e indicates a linear scaling of emission intensity with concentration within the 0.025 mg/mL and 0.25 mg/mL range. The data is consistent with interparticle self-quenching not being present for the 100 nm nanoshells but interparticle self-quenching being present for the 2µm microshells (Fig. 4d). Therefore, despite similar dye mass loading, the 100 nm nanoshells were found to be significantly brighter than the 2µm microshells at all concentrations tested. In order to better understand the underlying cause for this difference, TEM-EELS elemental mapping of the dye distribution on the shell walls was performed.

Fig. 5a depicts the region used for TEM-EELS mapping inscribed by

a blue rectangle on a TEM image of a nanoshells. Fig. 5b shows the TEM-EELS mapping of this region for carbon, which is expected to reflect the location of the ICG coating. Fig. 5c shows the oxygen elemental mapping, which reflects the location of the SiO₂ shell wall. The carbon signal appears on both sides of the shell wall and is non-uniform. In order to quantify these maps, multiple line scans were taken across an area with a width ≈ 9 nm in the center of the images in Fig. 4b and c. This line scan area is represented by a white bar. The averaged line scans for carbon are presented in Fig. 5d. Layer thickness was measured as the full width at half max (FWHM) of each peak after subtracting the background from the peak height. Carbon has a bimodal distribution, with a 2.6 nm layer on the exterior of the shell wall and a 0.9 nm layer on the interior of the shell. The minima between the C peaks correspond to the maxima of the O peaks (Fig. 5e). The data is consistent with formation of an inner ICG coating as well as an outer ICG coating. Since protein binding is known to quench ICG fluorescence in-vivo, the shielding of the internal ICG layer in the 100 nm nanoshells could extend the useful imaging lifetime in blood or serum rich tissues [24,25,40]. Additionally, the near monolayer coatings of dye found on the 100 nm nanoshells as well as their separation by an 8 nm silica shell results in a lower localized dye concentration, which has been shown to reduce the formation of energy traps (aggregates of dye molecules that decay absorbed energy non-radiatively) and, therefore, limit self-quenching between dye molecules on the same shell [44,45]. Previous studies with higher ICG dye loading than the present nanoshells and microshells have shown a that increasing localized ICG concentration on shells results in severe self-quenching [40]. This is consistent with the strong fluorescence shown in Fig. 4 for 100 nm nanoshells, since these have two very thin layers of ICG, self-quenching is minimized.

Fig. 6 presents the TEM-EELS elemental mapping for the 2µm microshells. Fig. 6a shows a TEM image of the shell wall with the elemental mapping area enclosed by a blue square. In order to avoid possible complications from imaging through a shell too thick in the plane of the beam, mapping was performed on a broken microshell. The contour of the opening is seen as a discrete change in contrast on the right side of the microshell. Fig. 6b shows the elemental mapping of C on the 2µm microshells. A single discrete layer of carbon is visible, and only located on the outside of the shell. On the right side of the shell, the layer seems to become more diffuse, likely due to imaging at the edge of the shell breakage, as highlighted in Fig. 6a. Since this region was outside the analyzed area, it did not affect the results. Fig. 6c shows the oxygen elemental mapping, which reflects the location of the SiO₂ shell wall. The averaged line scan shown in Fig. 6d reflects the unimodal distribution of carbon on the 2µm microshells with a single 6.1 nm thick exterior ICG layer. The ICG layer overlaps with the shell slightly, consistent with attachment to less dense silica layers which have previously been shown to be on the exterior of the shell [39]. Fig. 6e shows the averaged line scans for oxygen. Previously, the for 2µm microshells were shown to have a low density flaky exterior silica layer and a denser inner layer [39]. The gradual rise of the O signal is consistent with the shell becoming denser towards the center. The ICG dye adsorption penetrates the less dense exterior silica layer, but not through the entire thickness of the shell. The 2µm microshells have much thicker shell walls (24 nm vs 8 nm for the 100 nm nanoshells), consistent with ICG dye not being able to reach the inner hollow space. Formation of a single thicker layer only on the exterior of the 2µm microshells results in a much higher probability of self-quenching by energy traps within the thick layer, and, therefore, consistent with the lower luminescence compared to the 100 nm shells in the emission tests of Fig. 4 for equivalent mass loadings of ICG dye [40,44,45].

3.2. Ex vivo imaging penetration depth

Tumor resection margins are typically about 1 cm; therefore, imaging of fluorescent dye marker injections 1 cm deep in tissue is often required. To evaluate penetration through tissue, ICG coated nanoshells

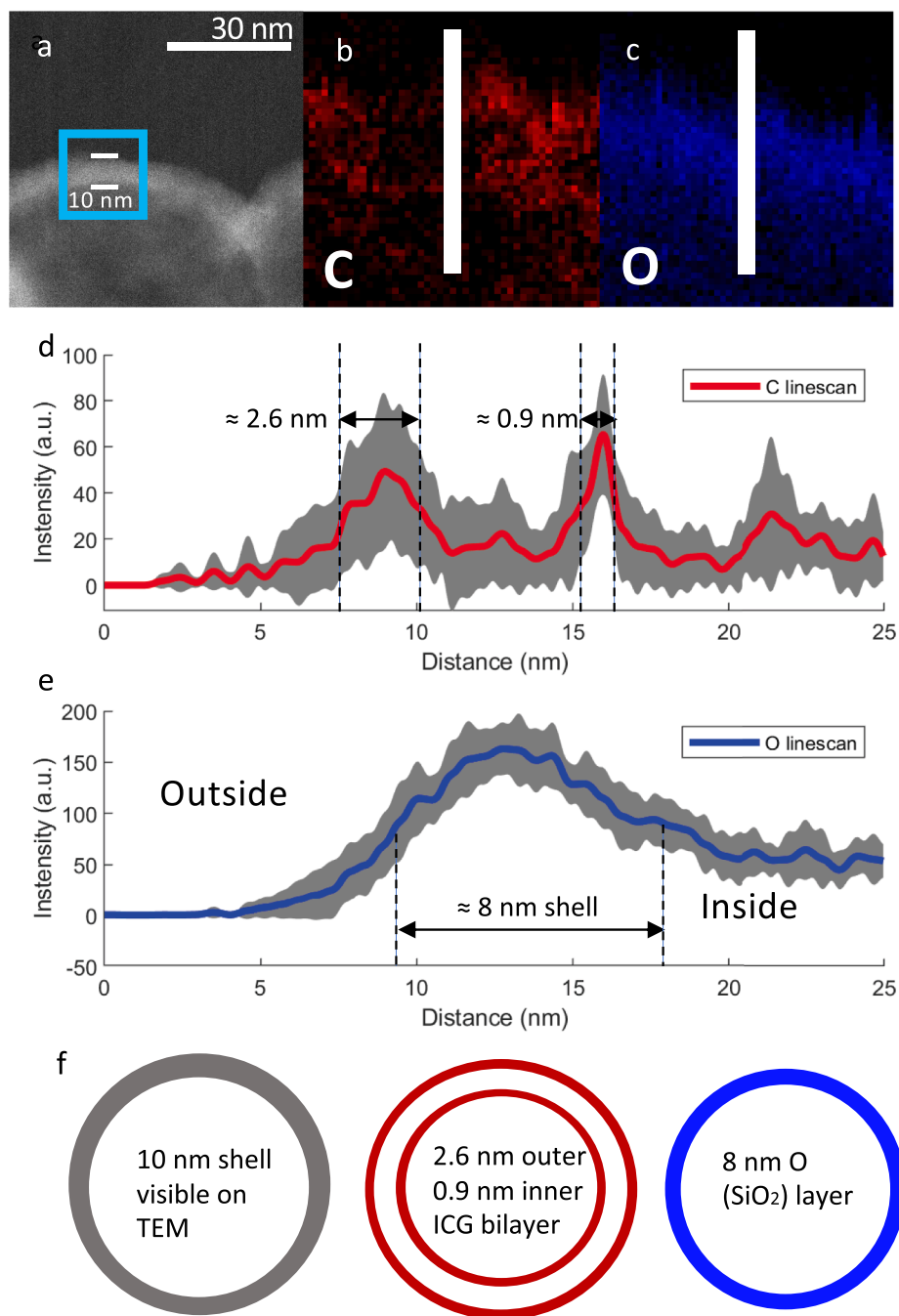


Fig. 5. TEM-EELS elemental mapping for 100 nm nanoshells. (a) TEM image of ICG coated 100 nm shell with the TEM-EELS mapping region highlighted in the blue box and shell thickness of 10 nm measured between the white bars; (b) Elemental map of C on the shell wall by TEM EELS; (c) Elemental map of O on shell wall. The linescan area analyzed is represented by the white bar. (d) The averaged linescan of C on shell wall. A ≈ 2.6 nm exterior ICG layer and 0.9 nm interior ICG layer can be seen; (e) Linescan of O on shell wall. Gray areas around the linescans represent standard deviations. Repeat linescans of a 9 nm wide section of shell in the middle of the images were used for averaging as well as calculation of standard deviations. (f) Schematic subdividing the shell wall into an external 2.6 nm ICG coating, the intact 8 nm SiO_2 shell and an internal 0.9 nm ICG coating.

were suspended in DI water at 0.25 mg/mL and covered with several layers of chicken or beef tissue. Each additional layer (average thickness of 5 mm for both beef and chicken) represents a step (Δx) increase in imaging depth. The distance between the IR camera and the sample was fixed at ≈ 15 cm.

A schematic representation of this experimental setup is shown in Fig. 7a. Fig. 7b shows the decrease in intensity of the emission (normalized to the emission of uncovered ICG coated nanoshells) as imaging depth increased. All images were captured at 200 ms exposure. The intensity decays in an exponential fashion, with a faster decay in optically denser beef tissue than chicken. Under chicken breast, emission was clearly visible up to ≈ 1.5 cm while under beef tissue, the emission was visible up to ≈ 1 cm. Therefore, ICG coated nanoshells are expected to be visible under up to 1 cm of tissue under clinically relevant imaging conditions, ensuring the ability of the surgeon to accurately

mark shallow sub-surface tumors. Sample images of the tissue slices in Fig. 7a are shown in Fig. S5.

3.3. In vivo toxicity

A complete blood count was performed on mice injected IV with 150 mg/kg of plain 100 nm silica nanoshells. As shown in Fig. S6, all values appeared to be within the reference range except for a lowered platelet count, which has previously been reported for silica shells but is expected to be dose dependent [46]. Because intratumoral injections for particles of this size are expected to remain fixed in the tumor and a lower dose was used for tumor marking (25 mg/kg), the systemic concentration for tumor marking would be considerably lower than what was used IV to study toxicity.

These results agree with existing literature for silica nanoparticles.

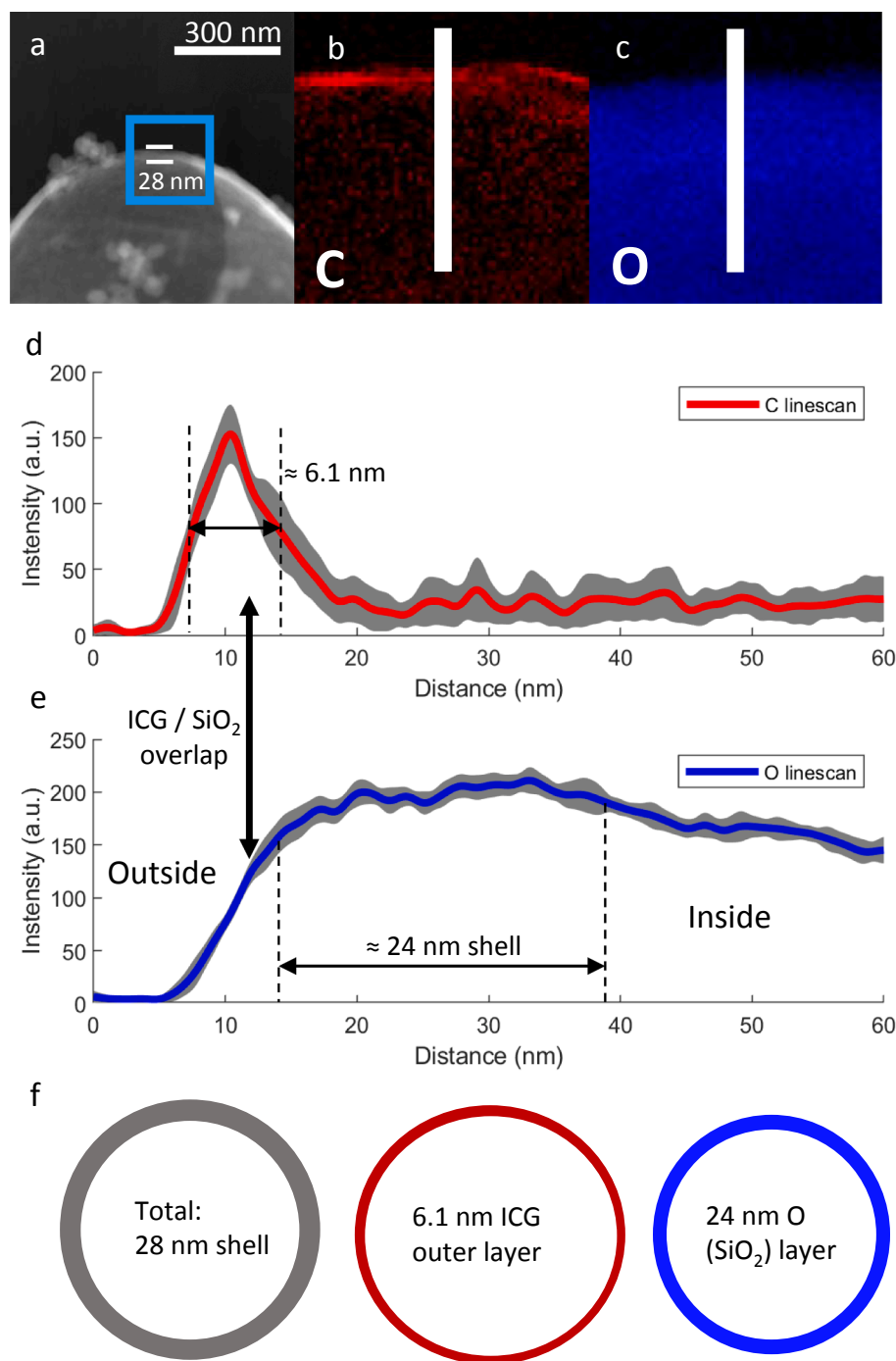


Fig. 6. TEM-EELS mapping for 2 μm microshells. (a) TEM image of ICG coated 100 nm shell with the TEM-EELS mapping region highlighted in the blue box and shell thickness of 10 nm measured between the white bars; (b) Elemental map of C on the shell wall by TEM EELS; (c) Elemental map of O on shell wall. The linescan area analyzed is represented by the white bar. (d) The averaged linescan of C on shell wall. A ≈ 2.6 nm exterior ICG layer and 0.9 nm interior ICG layer can be seen; (e) Linescan of O on shell wall. Gray areas around the linescans represent standard deviations. Repeat linescans of a 9 nm wide section of shell in the middle of the images were used for averaging as well as calculation of standard deviations. (f) Schematic subdividing the shell wall into an external 2.6 nm ICG coating, the intact 8 nm SiO₂ shell and an internal 0.9 nm ICG coating. Raw data for a single linescan is shown in Fig. S2.

Lu et al. studied the biocompatibility of silica nanoparticles and reported no significant changes in behavior, hematology or histology after a dose of 1 mg/(mouse-day) over a term of two months. Lu et al. also tested acute toxicity by injecting doses ranging from 10 mg/kg to 200 mg/kg. The only abnormality noted was slightly elevated liver transaminase aspartate aminotransferase (AST) for doses higher than 50 mg/kg [47]. This is considerably higher than the dose used for tumor marking in the present study (25 mg/kg).

There are also previous reports on toxicity of ICG coated silica shells. Hong et al. performed in vitro cytotoxicity testing with ICG coated silica shells with a higher ICG loading than the ones used in this study, finding minimal cytotoxicity [40]. Because ICG is FDA approved and considered to be very safe, it is not surprising that addition of ICG to silica particles would not adversely change their safety profile [11,48].

3.4. In vivo tumor marking

One potential advantage of ICG/HSS over free ICG dye is reduced leakage through tissue. It is well established in literature that free ICG dye clears rapidly from circulation and accumulates primarily in the liver [24,25,49]. Therefore, any long-term tumor marker employing ICG should seek to anchor the dye to the injection site and avoid diffusion into systematic circulation.

To test the spatial stability of ICG coated silica shells, the brighter 100 nm nanoshells and equivalent concentration (by mass of ICG) of free ICG dye were injected into tumor bearing mice. Tumors were grown at depths of 0.25 cm to 0.5 cm and the injected nanoshells were easily visible at these injection depths. Due to limitations in the animal model, tumors at larger depths were not tested.

The brightness of the tumor mark was imaged under the IR camera

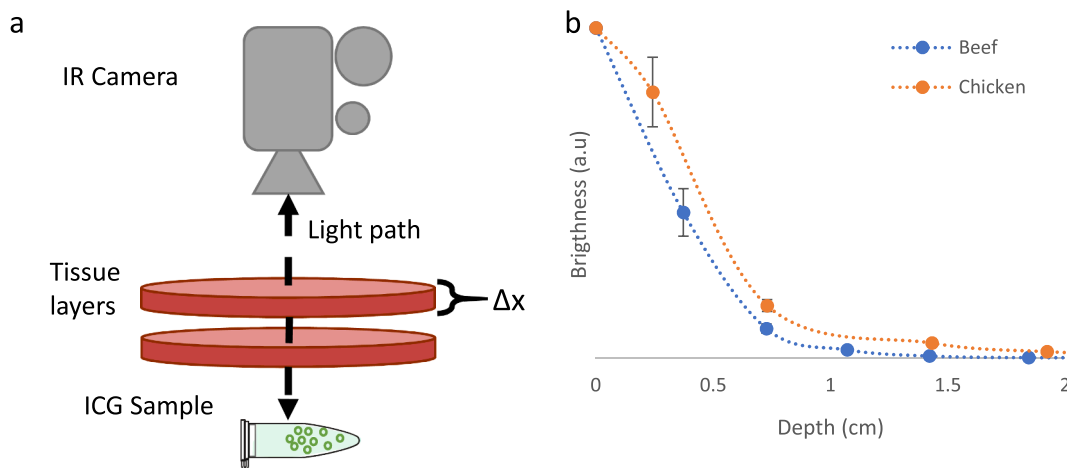


Fig. 7. Tissue penetration of 100 nm: (a) Schematic describing the experimental setup used to test tissue penetration ex-vivo. An Eppendorf tube was placed a fixed distance from an IR camera, and then thin layers of tissue are placed in the path of the illumination beam. (b) Intensity decay profile using chicken or beef as phantom tissue. Visibility was observed to be up to ≈ 1.5 cm using chicken and ≈ 1 cm using beef. Sample images from the stack shown in (a) are available in Fig. S3.

at days 0, 3, 7, 10, 13, 15, 18 and 21. For each image, the emission profile was fitted to a Cauchy probability distribution function to quantify the change in emission profile with time. Only images from days 0, 3, 7 and 10 were fit, because after this the signal was not bright enough to reliably fit the probability distribution function in some of the mice.

Fig. 8a shows a visible light image of the experimental setup used for IR imaging. Tumor bearing mice that were previously injected with either free ICG dye or ICG coated nanoshells are anesthetized and placed at a standard distance from the IR camera. Images are captured at several exposures using IR illumination and imaging, as well as with a single visible light image to calibrate dimensions and locate the tumor in dim IR images. Fig. 8b shows the emission and fitted emission profile for a free ICG dye mark 10 days after injection. Although the injection site can still be distinguished, the emission appears broad, indicative of diffusion of the dye through tissue. The fit to a Cauchy distribution is plotted as a white dotted line (enlarged for viewing, not to scale) and reveals an average FWHM of over 1 cm for free ICG dye. Fig. 8c shows the emission for ICG coated nanoshells. The emission from the nanoshells is brighter and narrower, allowing immediate and precise localization of the injection site. Fit to a Cauchy probability distribution (shown as a dotted white line, not to scale) reveals an average FWHM of 0.4 cm for ICG coated nanoshells.

The change in emission profile over time is shown in Fig. 8d. After 10 days, the emission profile of the ICG coated nanoshells remained unchanged and was considerably narrower than the emission profile of the free ICG dye ($p < 0.05$). For free ICG dye, diffusion through tissue results in loss of precision as a tumor marking agent if surgical excision is not performed within a few days of marking. Conversely, ICG coated nanoshells did not exhibit diffusion through tissue and their emission remained anchored to the site of injection and visible up to 10 days after initial delivery.

Raw intensity of emission was also compared between days 3 and 21 and is plotted in Fig. S7. Fig. S7a shows ICG coated nanoshells are significantly brighter than free ICG dye between day 7 and 15 ($p < 0.05$), although there is a decay in signal for both groups towards day 21. This decay in signal for the ICG nanoshells is likely related to the degradation of ICG in water (Fig. S3) as well as tumor progression (Fig. S8).

Protection of ICG dye from chemical degradation is an active area of research. Encapsulation into a hydrophobic polymer or perfluorocarbon

has been shown to greatly reduce photobleaching and degradation of ICG dye [50–53]. Application of these techniques to the formulation presented in this study could result in further improvement to the imaging lifetime.

Additionally, as shown in Fig. S8c, the tumors that grew rapidly lost the most IR fluorescent signal. This would not be expected to occur in patients since human tumors usually take months or years to grow, as opposed to < 2 weeks in this animal model. Future studies might benefit from use of a slower growing tumor model and protection of the dye on the shells from chemical degradation.

4. Conclusion

While free ICG dyes have been proposed for use in tumor marking, free ICG dye suffers from diffusion through tissue leading to shorter imaging persistence, thereby reducing the accuracy of tumor localization over time. Silica nanoshells were used as a potential carrier for ICG dye in order to securely anchor it to the injection site and shield the ICG dye from interaction with serum proteins and other biological factors that could reduce emission or degrade the dye.

Bright ICG-based tumor markers were synthesized by non-covalently bonding ICG to the surface of hollow silica microshells and nanoshells using electrostatic attraction between the negatively charged sulfonic groups on the ICG molecule and the positively charged amine group on surface functionalized silica shells. Elemental mapping with TEM-EELS showed dual thin layers (< 3 nm) of dye on the inside and outside of the 100 nm nanoshells, which greatly enhances emission brightness compared to the thicker exterior coating on larger $2\mu\text{m}$ microshells. This effect is consistent with avoiding self-quenching from formation of energy traps, as has been observed with high local concentrations of dye on shell surfaces, as well as protection of the inner shell ICG layer from quenching by interaction with proteins.

In-vitro and in-vivo tests documented that these ICG coated 100 nm silica nanoshells can be observed by IR fluorescence when injected at 1 cm depth into tissue and exhibit a persistent bright signal that lasts over 10 days, with negligible diffusion through tissue. At day 10, the ICG coated nanoshells were significantly brighter than free ICG dye, which lost more signal and diffused to the surrounding tissue. This presents a new method of marking tumors by anchoring a biocompatible dye to the injection site using a hard-shelled silica particle with a clear path for future improvement.

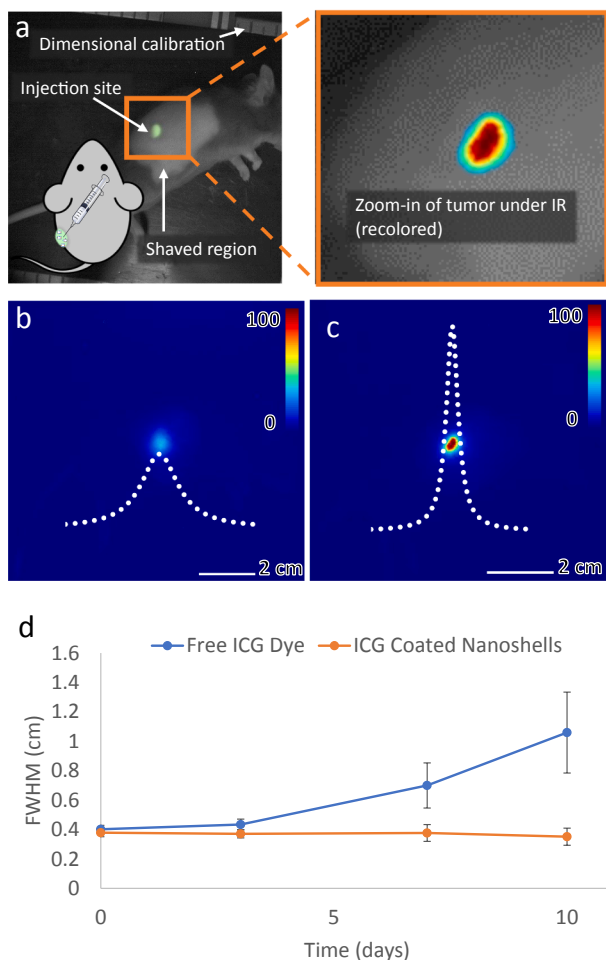


Fig. 8. Changes in emission profile over time of injection into mice tumors. (a) Visible light image of mouse during IR imaging. The green area is the injection site. The region surrounding the injection site was kept shaved to avoid signal loss due to hair growth during the experiment. The zoomed in panel shows how the NIR images in (b) and (c) relate to the injection site. (b) Emission profile for free ICG dye at day 10. The emission is diffuse and the peak is low in intensity. (c) Emission profile of 100 nm ICG coated nanoshells at day 10. The emission is highly localized, with a clearly delineated injection region. The Cauchy PDF line of best fit is shown in dotted white. Lines of best fit are enlarged for viewing and are not to scale. (d) Evolution of the FWHM of the emission profile over time. Free ICG dye diffuses through tissue, increasing the FWHM of the emission while ICG coated nanoshells maintain the same emission profile. At day 10, free ICG emission profiles are broader than that of coated shells ($p < 0.05$).

Acknowledgments and funding

Adrian Garcia Badaracco received funding from the Emerging Technologies Continuing Umbrella of Research Experience (ET CURE), a National Cancer Institute sponsored program. Grant number P30CA023100-28S.

James Wang's work was funded by the Center for Cross Training Translation Cancer Researchers in Nanotechnology, based out of the Moores Cancer Center of the University of California, San Diego. Grant number T32CA153915.

Erin Ward's work was funded by the NIH-NCI grant R33CA177449.

Additional funding was received from Viewpoint Medical Inc. (San Clemente, CA).

Declaration of competing interest

Sarah Blair's spouse is a co-founder, CEO and has equity interest in Viewpoint Medical. The terms of this arrangement have been reviewed and approved by the University of California, San Diego in accordance with its conflict of interest policies.

Andrew Kummel and William Trogler are stock holders, scientific advisory board members and scientific co-founders of Viewpoint Medical. The terms of this arrangement have been reviewed and approved by the University of California, San Diego in accordance with its conflict of interest policies.

Appendix A. Supplementary data

Supplementary data to this article can be found online at <https://doi.org/10.1016/j.apsusc.2019.143885>.

References

- [1] G. Munegato, et al., The diagnosis of non-palpable lesions in laparoscopic surgery of the colon, *Chir. Ital.* 55 (5) (2003) 657–661.
- [2] J. Yeung, C. Maxwell-Armstrong, A. Acheson, Colonic tattooing in laparoscopic surgery—making the mark? *Color. Dis.* 11 (5) (2009) 527–530.
- [3] M. Watanabe, et al., Colonic tattooing using fluorescence imaging with light-emitting diode-activated indocyanine green: a feasibility study, *Surg. Today* 39 (3) (2009) 214–218.
- [4] C.S. Bang, et al., Colonic abscess induced by India ink tattooing, *The Korean Journal of Gastroenterology* 64 (1) (2014) 45.
- [5] E. Coman, et al., Fat necrosis and inflammatory pseudotumor due to endoscopic tattooing of the colon with India ink, *Gastrointest. Endosc.* 37 (1) (1991) 65–68.
- [6] D. Gianom, A. Hollinger, H.P. Wirth, Intestinal perforation after preoperative colonic tattooing with India ink, *Swiss Surg.* 9 (6) (2003) 307–310.
- [7] C. Luigiano, et al., Endoscopic tattooing of gastrointestinal and pancreatic lesions, *Adv. Ther.* 29 (10) (2012) 864–873.
- [8] T. Elarini, S.D. Wexner, G.A. Isenberg, The need for standardization of colonoscopic tattooing of colonic lesions, *Dis. Colon Rectum* 58 (2) (2015) 264–267.
- [9] L.M. Fernandez, et al., How accurate is preoperative colonoscopic localization of colonic neoplasia? *Surg. Endosc.* (2018) 1–6.
- [10] R. Benson, H. Kues, Fluorescence properties of indocyanine green as related to angiography, *Phys. Med. Biol.* 23 (1) (1978) 159.
- [11] G.C. Taichman, P.J. Hendry, W.J. Keon, The use of cardio-green for intraoperative visualization of the coronary circulation: evaluation of myocardial toxicity, *Tex. Heart Inst. J.* 14 (2) (1987) 133.
- [12] J. Malicka, et al., Metal-enhanced emission from indocyanine green: a new approach to in vivo imaging, *J. Biomed. Opt.* 8 (3) (2003) 472–478.
- [13] M. Landsman, et al., Light-absorbing properties, stability, and spectral stabilization of indocyanine green, *J. Appl. Physiol.* 40 (4) (1976) 575–583.
- [14] X. Li, et al., Tumor localization using fluorescence of indocyanine green (ICG) in rat models, *Optical Tomography, Photon Migration, and Spectroscopy of Tissue and Model Media: Theory, Human Studies, and Instrumentation*, International Society for Optics and Photonics, 1995.
- [15] J.T. Alander, et al., A review of indocyanine green fluorescent imaging in surgery, *Journal of Biomedical Imaging* 2012 (2012) 7.
- [16] A. de la Zerda, et al., Family of enhanced photoacoustic imaging agents for high-sensitivity and multiplexing studies in living mice, *ACS Nano* 6 (6) (2012) 4694–4701.
- [17] X. Yang, et al., Nanoparticles for photoacoustic imaging, *Wiley interdisciplinary reviews: nanomedicine and nanobiotechnology* 1 (4) (2009) 360–368.
- [18] H. Wang, et al., In vivo photoacoustic molecular imaging of breast carcinoma with folate receptor-targeted indocyanine green nanoprobes, *Nanoscale* 6 (23) (2014) 14270–14279.
- [19] W.R. Chen, et al., Photothermal effects on murine mammary tumors using indocyanine green and an 808-nm diode laser: an in vivo efficacy study, *Cancer Lett.* 98 (2) (1996) 169–173.
- [20] J. Yu, et al., Self-assembly synthesis, tumor cell targeting, and photothermal capabilities of antibody-coated indocyanine green nanocapsules, *J. Am. Chem. Soc.* 132 (6) (2010) 1929–1938.
- [21] J. Yu, et al., Synthesis of near-infrared-absorbing nanoparticle-assembled capsules, *Chem. Mater.* 19 (6) (2007) 1277–1284.
- [22] R. Lv, et al., Stable ICG-loaded upconversion nanoparticles: silica core/shell theranostic nanoplatfor for dual-modal upconversion and photoacoustic imaging together with photothermal therapy, *Sci. Rep.* 7 (1) (2017) 15753.
- [23] C. Abels, et al., Indocyanine green and laser light for the treatment of AIDS-associated cutaneous Kaposi's sarcoma, *Br. J. Cancer* 77 (6) (1998) 1021–1024.
- [24] T. Desmettre, J. Devoisselle, S. Mordon, Fluorescence properties and metabolic

- features of indocyanine green (ICG) as related to angiography, *Surv. Ophthalmol.* 45 (1) (2000) 15–27.
- [25] C.H. Lee, et al., Near-infrared mesoporous silica nanoparticles for optical imaging: characterization and in vivo biodistribution, *Adv. Funct. Mater.* 19 (2) (2009) 215–222.
- [26] J. Nagata, et al., Colonic marking with near-infrared, light-emitting, diode-activated Indocyanine green for laparoscopic colorectal surgery, *Dis. Colon Rectum* 59 (2) (2016) e14–e18.
- [27] J.G. Lee, A.H. Low, J.W. Leung, Randomized comparative study of indocyanine green and India ink for colonic tattooing: an animal survival study, *J. Clin. Gastroenterol.* 31 (3) (2000) 233–236.
- [28] N. Miyoshi, et al., Surgical usefulness of indocyanine green as an alternative to India ink for endoscopic marking, *Surg. Endosc.* 23 (2) (2009) 347–351.
- [29] A.R. e Sousa, et al., Self-quenching of azulene fluorescence in cyclohexane, *J. Photochem. Photobiol. A Chem.* 83 (3) (1994) 199–203.
- [30] H. Mok, et al., Indocyanine green encapsulated nanogels for hyaluronidase activatable and selective near infrared imaging of tumors and lymph nodes, *Chem. Commun.* 48 (69) (2012) 8628–8630.
- [31] E.I. Altinoğlu, et al., Near-infrared emitting fluorophore-doped calcium phosphate nanoparticles for in vivo imaging of human breast Cancer, *ACS Nano* 2 (10) (2008) 2075–2084.
- [32] A. Liberman, et al., Hollow silica and silica-boron nano/microparticles for contrast-enhanced ultrasound to detect small tumors, *Biomaterials* 33 (20) (2012) 5124–5129.
- [33] A. Liberman, et al., Synthesis and surface functionalization of silica nanoparticles for nanomedicine, *Surf. Sci. Rep.* 69 (2) (2014) 132–158.
- [34] A. Liberman, et al., Color doppler ultrasound and gamma imaging of intratumorally injected 500 nm iron-silica nanoshells, *ACS Nano* 7 (7) (2013) 6367–6377.
- [35] C.N. Ta, et al., Integrated processing of contrast pulse sequencing ultrasound imaging for enhanced active contrast of hollow gas filled silica nanoshells and microshells, *J. Vac. Sci. Technol. B* 30 (2) (2012) 02C104.
- [36] J. Yang, J.U. Lind, W.C. Trogler, Synthesis of hollow silica and titania nanospheres, *Chem. Mater.* 20 (9) (2008) 2875–2877.
- [37] J. Yang, et al., Ultrasound responsive macrophase-segregated microcomposite films for in vivo biosensing, *ACS Appl. Mater. Interfaces* 9 (2) (2017) 1719–1727.
- [38] J. Yang, et al., Silica shells/adhesive composite film for color Doppler ultrasound guided needle placement, *ACS Biomater. Sci. Eng.* 3 (2017) 1780.
- [39] A. Liberman, et al., Mechanically tunable hollow silica ultrathin Nanoshells for ultrasound contrast agents, *Adv. Funct. Mater.* 25 (26) (2015) 8.
- [40] S. ho Hong, H. Kim, Y. Choi, Indocyanine green-loaded hollow mesoporous silica nanoparticles as an activatable theranostic agent, *Nanotechnology* 28 (18) (2017) 185102.
- [41] N. Mendez, et al., Assessment of in vivo systemic toxicity and biodistribution of iron-doped silica nanoshells, *Nanomedicine* 13 (3) (2017) 933–942.
- [42] V. Saxena, M. Sadoqi, J. Shao, Degradation kinetics of indocyanine green in aqueous solution, *J. Pharm. Sci.* 92 (10) (2003) 2090–2097.
- [43] Y. Zhu, et al., PEGylated hollow mesoporous silica nanoparticles as potential drug delivery vehicles, *Microporous Mesoporous Mater.* 141 (1–3) (2011) 199–206.
- [44] H.B. Rodriguez, E.S. Roman, Effect of concentration on the photophysics of dyes in light-scattering materials, *Photochem. Photobiol.* 89 (6) (2013) 9.
- [45] H.B. Rodriguez, et al., Photophysics at unusually high dye concentrations, *Acc. Chem. Res.* 52 (1) (2019) 8.
- [46] J.J. Corbalan, et al., Amorphous silica nanoparticles aggregate human platelets: potential implications for vascular homeostasis, *International Journal of Nanomedicine* 7 (2012) 631.
- [47] J. Lu, et al., Biocompatibility, biodistribution, and drug-delivery efficiency of mesoporous silica nanoparticles for cancer therapy in animals, *Small* 6 (16) (2010) 1794–1805.
- [48] G. Ferrauto, et al., Large photoacoustic effect enhancement for ICG confined inside MCM-41 mesoporous silica nanoparticles, *Nanoscale* 9 (1) (2017) 99–103.
- [49] W. Song, et al., Comprehensive studies of pharmacokinetics and biodistribution of indocyanine green and liposomal indocyanine green by multispectral optoacoustic tomography, *RSC Adv.* 5 (5) (2015) 3807–3813.
- [50] V.B. Rodriguez, et al., Encapsulation and stabilization of indocyanine green within poly(styrene-alt-maleic anhydride) block-poly(styrene) micelles for near-infrared imaging, *J. Biomed. Opt.* 13 (1) (2008) 1–10 (10).
- [51] A. Schönbacher, et al., Indocyanine green loaded biocompatible nanoparticles: stabilization of indocyanine green (ICG) using biocompatible silica-poly(ϵ -caprolactone) grafted nanocomposites, *J. Photochem. Photobiol. A Chem.* 261 (2013) 12–19.
- [52] N. Beziere, et al., Dynamic imaging of PEGylated indocyanine green (ICG) liposomes within the tumor microenvironment using multi-spectral optoacoustic tomography (MSOT), *Biomaterials* 37 (2015) 415–424.
- [53] B. Quan, et al., Near infrared dye indocyanine green doped silica nanoparticles for biological imaging, *Talanta* 99 (2012) 387–393.